electronics

MDPI

Article

Effects of Diffusion Barrier Layers on the Performance of Lattice-Mismatched Metamorphic $In_{0.83}Ga_{0.17}As$ Photodetectors

Zhejing Jiao [1], Tianyu Guo [1], Gaoyu Zhou [1], Yi Gu [2,*], Bowen Liu [2], Yizhen Yu [2], Chunlei Yu [2], Yingjie Ma [2], Tao Li [2] and Xue Li [2]

[1] College of Electronics and Information Engineering, Shanghai University of Electric Power, Shanghai 201306, China; zhejing.jiao@shiep.edu.cn (Z.J.); gty990928@163.com (T.G.); 18552976220@163.com (G.Z.)

[2] Shanghai Institute of Technical Physics, Chinese Academy of Sciences, Shanghai 200083, China; liubowen@mail.sitp.ac.cn (B.L.); yuyizhen@mail.sitp.ac.cn (Y.Y.); yuchunlei@mail.sitp.ac.cn (C.Y.); mayingjie@mail.sitp.ac.cn (Y.M.); litao@mail.sitp.ac.cn (T.L.); lixue@mail.sitp.ac.cn (X.L.)

* Correspondence: guyi@mail.sitp.ac.cn

Abstract: In the planar-type InGaAs photodetector (PD) structure, a diffusion barrier has the effect of modifying the zinc diffusion profile in the interface between the cap and the absorption layer to improve device performance. In this work, an n-type $In_{0.83}Ga_{0.17}As$ diffusion barrier layer (DBL) is employed between the $In_{0.83}Al_{0.17}As$ cap layer and the low-doped $In_{0.83}Ga_{0.17}As$ absorption layer of a lattice-mismatched metamorphic $In_{0.83}Ga_{0.17}As$ PD. The device performance of the $In_{0.83}Ga_{0.17}As$ PDs in terms of dark current, quantum efficiency, and capacitance were simulated and compared to experimental results. The effects of the thickness and doping concentration of the DBL on PD performance were analyzed and shown to be optimized at both 300 K and 200 K. Based on the simulation results, the electron concentration of the DBL is recommended to be 3×10^{16}–5×10^{16} cm^{-3} and a thickness of 0.1 μm is suggested.

Keywords: diffusion barrier layer; metamorphic $In_{0.83}Ga_{0.17}As$ photodetector; latticed-mismatched; dark current

Citation: Jiao, Z.; Guo, T.; Zhou, G.; Gu, Y.; Liu, B.; Yu, Y.; Yu, C.; Ma, Y.; Li, T.; Li, X. Effects of Diffusion Barrier Layers on the Performance of Lattice-Mismatched Metamorphic $In_{0.83}Ga_{0.17}As$ Photodetectors. *Electronics* **2024**, *13*, 1339. https://doi.org/10.3390/electronics13071339

Academic Editor: Longqing Cong

Received: 25 February 2024
Revised: 20 March 2024
Accepted: 29 March 2024
Published: 2 April 2024

1. Introduction

InP-based InGaAs alloys are characterized by their elevated absorption coefficients, enhanced electron mobility, superior physicochemical stability, and robust resistance to radiation exposure. The photodetectors (PDs) fabricated using these alloys exhibit a range of advantageous properties, including elevated operational temperatures, heightened quantum efficiency, and augmented sensitivity [1–3]. These attributes render them a significant option for applications in short-wave infrared (SWIR) detection. In near-wave infrared (NWIR) detection, the design and fabrication of high performance InGaAs PDs has been previously reported [4]. High-indium (In) $In_xGa_{1-x}As$ ($x > 0.53$) PDs covering the longer part of the SWIR wavelength (1.7–3 μm) range have attracted much attention in remote sensing, including in applications such as Earth resource observation, environmental monitoring, and night vision [5–9]. InGaAs PDs are favored due to their high sensitivity, rapid response time, and superior performance in the near-infrared region. One of the crucial concerns with InGaAs-based SWIR PDs is the lattice mismatch between the high-In InGaAs absorption layer and the InP substrate. For metamorphic InGaAs PDs, InGaAs with In content of 0.85 grown on GaAs substrates using an interfacial misfit array-based simple buffer has been previously reported [10]. The lattice mismatch rises up to about 2.5% for the InGaAs with In content of 0.83. The deterioration in material quality caused by lattice mismatch constrains enhancements in device performance. To improve PD performance, various kinds of buffer structures [11–13] are used to mitigate the effects of lattice mismatch. Additionally, electron barriers such as AlGaAsSb [14] and superlattice

structures within the absorption layer [15] have also been reported. Moreover, the material structure of the infrared detector is adjusted by inserting layers for mid-wave infrared (MWIR) detection. High-performance $InAs_{0.91}Sb_{0.09}$ detectors decrease the dark current with the introduction of the $AlAs_{1-y}Sb_y$ graded barrier layer [16]. Further, nBn InAs/GaSb type-II superlattice PDs with a stepped absorber have been proposed to enhance the extraction of photogenerated carriers from the active layers [17]. The structural designs have been proven to be effective in improving PD performance.

For planar InGaAs PDs, the depth of the p-n junction in the InGaAs absorption layer is a critical parameter determining device performance, which usually involves a zinc diffusion process at the interface between the cap and absorption layers. Junction depth could be controlled by fine-tuning the diffusion temperature and time in the zinc diffusion process [18]. A highly doped diffusion barrier structure has been reported recently for lattice-matched $In_{0.53}Ga_{0.47}As$/InP PDs and was experimentally proved to effectively reduce the diffusion depth into the $In_{0.53}Ga_{0.47}As$ absorption layer [19]. PD performance with the diffusion barrier layer (DBL) has been analyzed; however, the thickness and the doping concentration of the DBL are fixed in the experiments and may not be applicable for lattice-mismatched $In_{0.83}Ga_{0.17}As$/InP PDs. The latticed-mismatched $In_{0.83}Ga_{0.17}As$/InP PD is observed to have a faster diffusion rate due to higher defect density, and the control of zinc diffusion is much more difficult [20]. An ideal zinc diffusion involves accurately placing the p/n interface at the hetero-structural interface between the cap layer and InGaAs absorption layer. The DBL is more required in the lattice-mismatched metamorphic InGaAs PD to induce a diffusion barrier with a lower diffusion rate at the interface, while a DBL with higher doping density could affect device performance and would need to be optimized.

In this work, the DBL structure is applied and optimized in lattice-mismatched metamorphic $In_{0.83}Ga_{0.17}As/In_{0.83}Al_{0.17}As$/InP PDs. The DBL is an n-type $In_{0.83}Ga_{0.17}As$ ternary alloy with the same In content as the $In_{0.83}Ga_{0.17}As$ absorption layer but a higher doping concentration. It is placed between the $In_{0.83}Al_{0.17}As$ cap layer and the $In_{0.83}Ga_{0.17}As$ absorption layer. The performance of the PD with the DBL is investigated at 300 K and 200 K through simulation. The thickness of the DBL is varied between 0 and 0.5 μm and the doping concentration between 1×10^{16} and 1×10^{17} cm^{-3}. Their effects on the dark current, quantum efficiency, and capacitance of the PD with the DBL are analyzed and compared to the PD without the DBL. The energy band diagram and the depletion region of the DBL structure are analyzed to provide explanations of the effect of the DBL. Lastly, optimal DBL thickness and doping concentration are provided based on the simulation results.

2. Materials and Methods

The PD with a DBL that was used for simulation is shown in Figure 1, and the corresponding material parameters for each layer are shown in Table 1.

Table 1. Material parameters of the simulated PD structure with the DBL.

Layer	Layer Thickness (μm)	Doping Concentration (cm^3)
n-$In_{0.83}Al_{0.17}As$ cap layer	0.6	3×10^{16}
n-$In_{0.83}Ga_{0.17}As$ DBL	0~0.5	$(0.1\sim1) \times 10^{17}$
n-$In_{0.83}Ga_{0.17}As$ absorption layer	2.5	5×10^{15}
n-InAlAs buffer layer	2.38	6.6×10^{17}
InP substrate	350	Semi-insulated

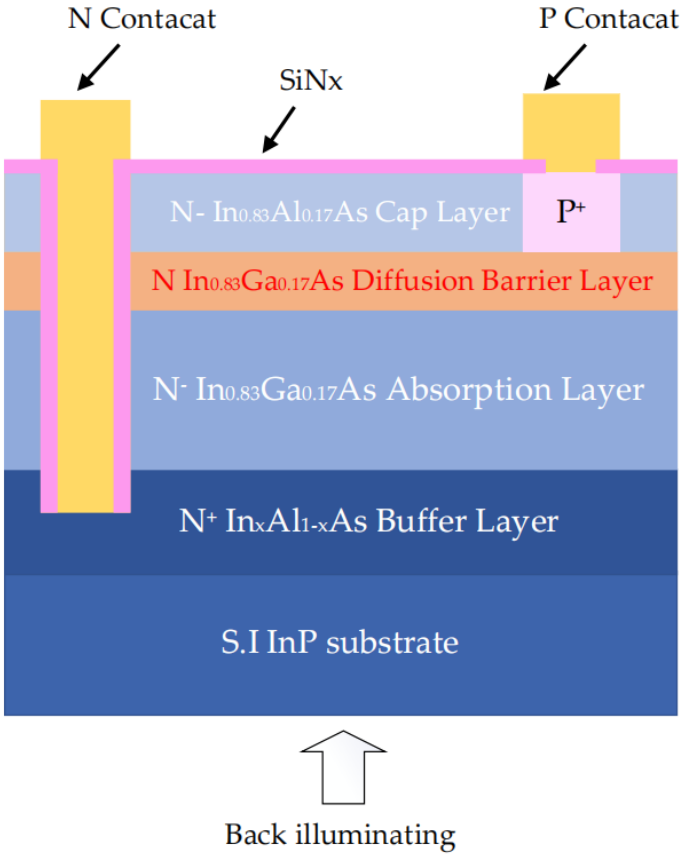

Figure 1. The simulated $In_{0.83}Ga_{0.17}As$/InP PD structure with the DBL between the absorption layer and the cap layer.

The simulated PD with the DBL consists of a 350 μm thick semi-insulated InP substrate, a 2.38 μm thick n-type (6.6×10^{17} cm^{-3}) $In_yAl_{1-y}As$ (y increases from 0.52 to 0.83) buffer layer, a slightly doped (5×10^{15} cm^{-3}) n-type $In_{0.83}Ga_{0.17}As$ absorption layer, an n-type $In_{0.83}Ga_{0.17}As$ DBL, and a 0.6 μm thick n-type (3×10^{16} cm^{-3}) $In_{0.83}Al_{0.17}As$ cap layer. A p-type doping well (2×10^{18} cm^{-3}) in the InAlAs cap layer is considered in the simulation and the size of the simulated PD structure is 20 μm × 20 μm. In addition to the simulation, an $In_{0.83}Ga_{0.17}As$ PD reference sample is demonstrated in experiments and compared to the simulation. The sample is the PD structure without the DBL, while the other layers are consistent with the simulated structure.

To investigate the performance of the PD with the DBL, the Atlas semiconductor modeling tools provided by Silvaco TCAD are adopted in the simulation. In the simulation, Shockley–Read–Hall (SRH), radiative, and Auger recombination mechanisms are included, which determine minority carrier lifetimes and affect dark current and photocurrent. The SRH lifetime of $In_{0.83}Ga_{0.17}As$ is set as 2×10^{-7} s at the doping concentration of 5×10^{15} at 300 K and decreased at higher doping concentrations and lower temperatures according to Ref. [21]. The radiative and Auger recombination coefficients of $In_{0.83}Ga_{0.17}As$ are taken to be 1.43×10^{-10} cm^3/s and 7×10^{-27} cm^6/s, respectively [22]. The material parameters for InP, $In_{0.83}Ga_{0.17}As$, and $In_{0.83}Al_{0.17}As$ in the simulation are shown in Table 2 [23–27]. The material parameters for InP are assumed to be default in the Atlas module. Regarding the simulation, the absorption coefficients of $In_{0.83}Ga_{0.17}As$ at 300 K are shown in Table 3 [21]. At 200 K, the absorption spectrum is blue-shifted and the intensity is slightly decreased [21]. The absorption coefficients of InAlAs are taken from Ref. [28]. The electron and hole mobilities are also considered to be concentration-dependent and temperature-dependent. The thicknesses of the DBL in the simulation are taken to be 0.05, 0.1, 0.2, 0.3, 0.4, and 0.5 μm and the doping concentration was set as 1×10^{16}, 3×10^{16}, 5×10^{16}, 8×10^{16}, and 1×10^{17} cm^{-3}. The thickness and concentration of the DBL on the

energy band diagram, the dark current, the quantum efficiency, and the capacitance of the PD were simulated and analyzed.

Table 2. Material parameters used for the simulation (300 K).

Material Parameters	InP [23]	$In_{0.83}Ga_{0.17}As$ [24–27]	$In_{0.83}Al_{0.17}As$
Bandgap (eV)	1.34	0.48	0.79
Electron density of states (cm^{-3})	5.66×10^{17}	1.20×10^{17}	2.61×10^{17}
Hole density of states (cm^{-3})	2.03×10^{17}	6.99×10^{18}	1.14×10^{19}
Electron mobility (cm^2/Vs)	4600	8000	3000
Hole mobility (cm^2/Vs)	150	112	100
SRH lifetime electron (s)	1×10^{-8}	2×10^{-7}	1×10^{-8}
SRH lifetime hole (s)	1×10^{-8}	2×10^{-7}	1×10^{-8}
Permittivity	12.5	14.63	13.96

Table 3. The absorption coefficients at specific photo energies of $In_{0.83}Ga_{0.17}As$ (300 K) [21].

hν (eV)	0.47	0.48	0.49	0.53	0.55	0.6	0.7	0.8
α (10^3 cm^{-1})	0.6	2.3	3.75	6.15	7	8.98	12.4	16.8

3. Results

3.1. The Energy Band Diagram

The energy band diagrams as a function of the thickness and the doping concentration of the DBL layer at the reverse bias of 0 V are shown in Figure 2.

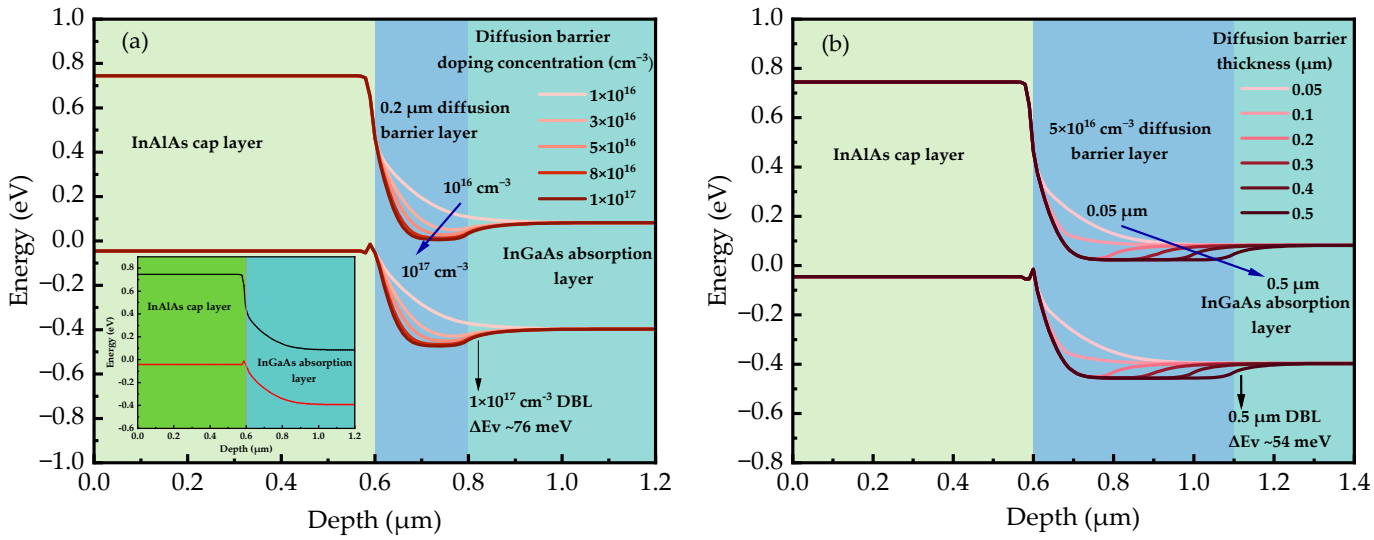

Figure 2. The energy band diagram as a function of (**a**) doping concentration (1×10^{16}, 3×10^{16}, 5×10^{16}, 8×10^{16}, and 1×10^{17} cm^{-3}) and (**b**) the thickness (0.05, 0.1, 0.2, 0.3, 0.4, and 0.5 μm) of the DBL at a biased voltage of 0 V. The inset shows the energy band diagram without the DBL at 0 V.

It can be seen that the DBL layer has a higher doping concentration than the absorption layer, forming a well shape between the InAlAs cap layer and the InGaAs absorption layer, which has the effect of accumulating carriers and impeding the transportation of carriers. With the increase in doping concentration from 1×10^{16} to 1×10^{17} cm^{-3}, the energy-band well gets deeper, as shown in Figure 2a. When DBL thickness is more than 0.1 μm, the well shape is also observed in Figure 2b. The band offsets between the DBL and the InGaAs absorption layer are marked in the figure. The band offsets for both the conduction and valence bands are the same at the InGaAs homojunction. In Figure 2a, the offset

increases with doping concentration and reaches 76 meV at the doping concentration of 1×10^{-7} cm^{-3}. In Figure 2b, the offset is maintained at 54 meV at DBL thicknesses beyond 0.1 µm. The conduction band offset can block minority electrons from the DBL moving to the InGaAs absorption layer, which has the advantage of reducing dark current, while the valence band offset can block the transportation of photo-generated holes from the InGaAs absorption layer, which has the disadvantage of decreasing quantum efficiency. From the band diagram, it is seen that the DBL could affect PD performance. Its thickness and doping concentration need to be carefully considered in the simulation. Thus, in the following sections we investigate the effect of the DBL on the dark current, quantum efficiency, and capacitance of PDs.

3.2. Dark Current Density

The dark current is an important characteristic parameter of a PD, which is usually correlated with material quality, carrier lifetime, and the carrier transportation of the device. Therefore, we simulated the influence of the DBL on the dark current at 300 K and 200 K.

Figure 3 shows the simulated temperature-dependent dark current density–voltage (J-V) curves for the PD structure with a 0.1 µm thick DBL doped at 5×10^{16} cm^{-3} at 300 K and 200 K. Additionally, the measured J-V curve of the InGaAs PD reference sample without the DBL is also plotted in Figure 3. At the reverse bias of −10 mV, the simulated dark current density values of the PD structure without the DBL and the PD with a 0.1 µm thick 5×10^{16} cm^{-3} DBL structure are about 1.43×10^{-4} A/cm^2 and 1.15×10^{-4} A/cm^2 at 300 K, respectively, while at 200 K, the values are about 4.01×10^{-7} A/cm^2 and 2.52×10^{-7} A/cm^2, respectively. The measured dark current density of the PD without the DBL is 4.84×10^{-4} A/cm^2 at −10 mV at 300 K and 3.49×10^{-7} A/cm^2 at −10 mV at 200 K in the experiments. It can be also seen that the simulated curve of the dark current density of the reference sample is only a little bit lower than the measured one at 300 K. The difference may be due to the surface dark current, which is not taken into account in the simulation. At 200 K, the measured curve almost overlaps with the simulated one, indicating a high degree of accuracy in our simulation parameters and models.

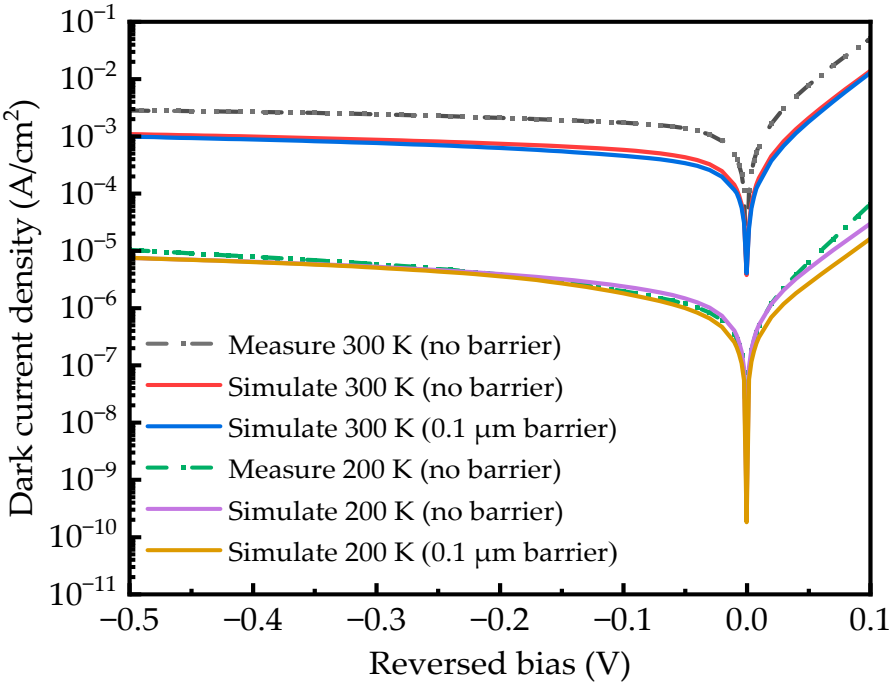

Figure 3. Simulated dark current density as a function of reversed bias for the PD with a 0.1 µm thick 5×10^{16} cm^{-3} DBL at 300 K and 200 K. The simulated and measured dark current densities for the PD without the DBL are also shown for comparison.

For the $In_{0.83}Ga_{0.17}As$ PDs, the dark current is composed of two main components: the diffusion current I_{diff} and the generation–recombination current I_{gr}. The energy bandgap E_g of $In_{0.83}Ga_{0.17}As$ is around 0.48 eV at 300 K, and the theoretical activation energy E_a for I_{diff} and I_{gr} have been determined to be E_g and $E_g/2$, respectively [29,30]. Therefore, we can calculate the theoretical E_a value to determine the dominant dark current at different temperature ranges by using the relationship of $J \propto exp(-Ea/kT)$, where J is the dark current density, E_a is the activation energy, k is the Boltzmanm constant, and T is the temperature.

Figure 4 shows the Arrhenius plots of the temperature-dependent dark currents at −10 mV for PDs with DBLs of different thicknesses at the doping concentration of 5×10^{16} cm^{-3}. Thermal activation energy E_a is obtained by linearly fitting the simulated data in Figure 4. The fitted E_a values are all close to 0.50 eV in the temperature range of 260–300 K, represented as E_1 in the figure, which is close to the $In_{0.83}Ga_{0.17}As$ bandgap of 0.48 eV, indicating a diffusion-dominant behavior in the temperature range of 260–300 K. On the other hand, the fitted E_a values are all close to 0.26 eV in the temperature range of 200–240 K, as represented by E_2 in the figure. This indicates that the generation–recombination current is the dominant dark current for this lower temperature range. Compared to the PD without the DBL, the dominant dark currents stay the same with the introduction of the DBL in the PD for the temperature range between 200 and 300 K.

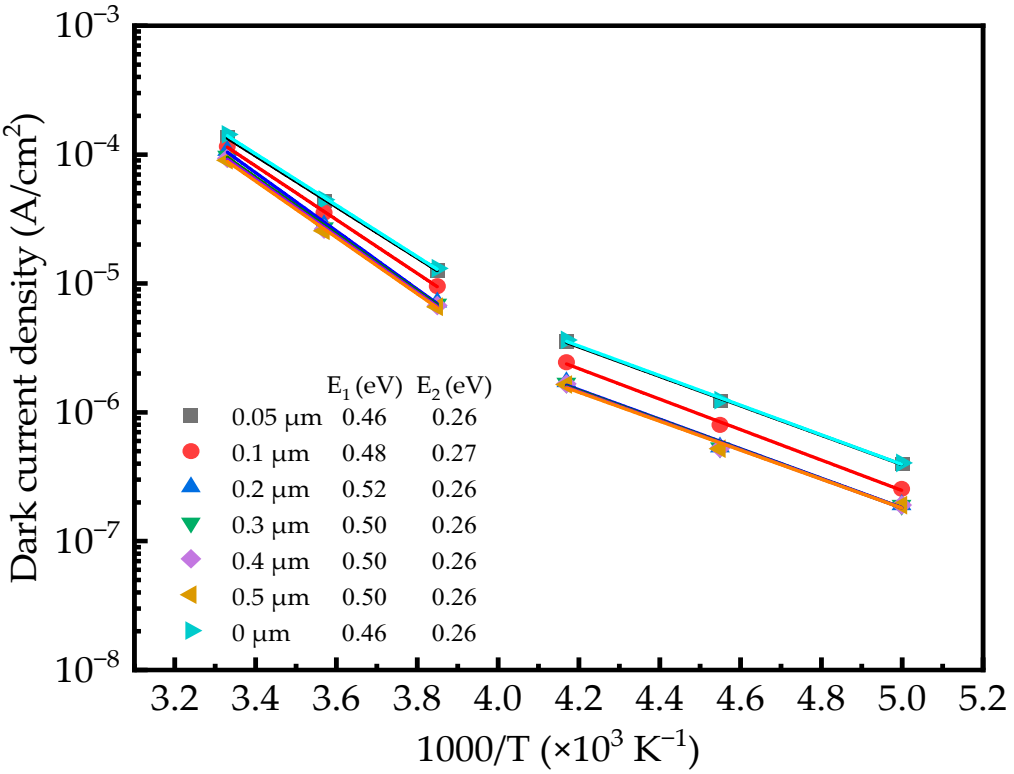

Figure 4. Dark current density as a function of 1000/T at −10 mV for the PD with the 5×10^{16} cm^{-3} DBL of different thicknesses. E_1 (260–300 K) and E_2 (200–240 K) represent the activation energies of the two temperature ranges.

The effects of the DBL on dark current density at 300 K and 200 K are shown in Figure 5. In general, dark current density decreases with increases in the thickness of the DBL, partly due to the well shape in the energy band diagram illustrated in Figure 2. At 0.05 and 0.1 μm, where the band offset is very small, the dark current density slightly decreases. By further increasing the thickness and doping concentration of the DBL, the band offset increases and the dark current density starts to decrease. Furthermore, with the doping concentration increase from 1×10^{16} to 3×10^{16} cm^{-3}, the dark current density decreases rapidly due

to smaller depletion width and an almost unchanged minority carrier lifetime that is dominated by SRH recombination at this doping range. With the doping concentration further increased to 1×10^{17} cm^{-3}, the downward trend becomes small and even reversed at the doping concentration of 8×10^{16} at 200 K due to the shortened minority carrier lifetime. At medium and high doping ranges, the minority carrier lifetimes are dominated by radiative and Auger recombinations, which are inversely proportional to the doping concentration and the square of the doping concentration, respectively [31]. When the thickness of the DBL is 0.05 µm, dark current density rarely decreases. From the perspective of the dark current, we suggest the doping concentration of the DBL should be between 3×10^{16} and 8×10^{16} cm^{-3} with the thicknesses between 0.1 and 0.5 µm.

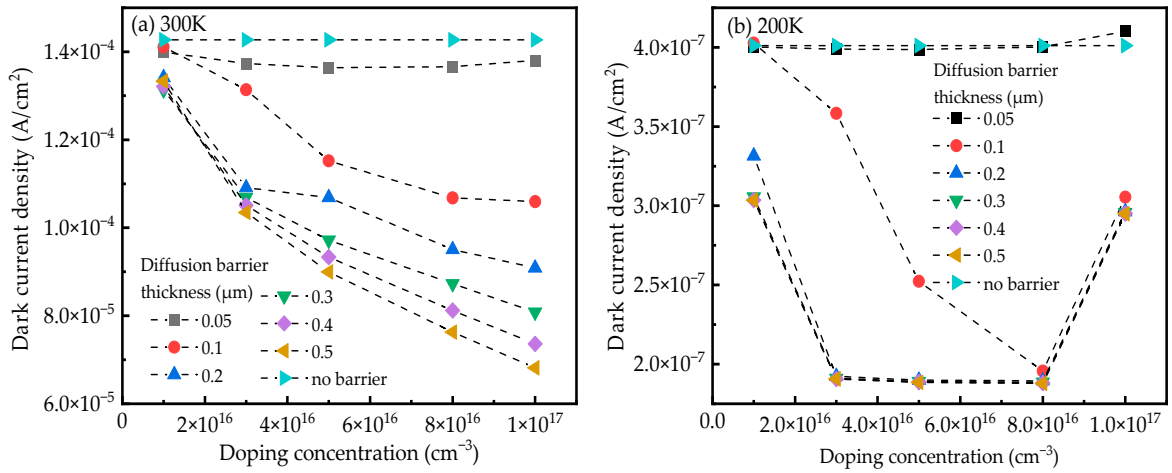

Figure 5. Dark current density as a function of doping concentration for different thicknesses of DBL at (**a**) 300 K and (**b**) 200 K. The dark current density of the PD structure without the DBL is also plotted for comparison.

3.3. Quantum Efficiency

Another important parameter of a PD is quantum efficiency. The effect of the DBL on quantum efficiency was also investigated through simulation. Optical light was illuminated from the back of the PD with a power density of 1 W/cm^2. The doping concentration of the DBL was fixed at 5×10^{16} cm^{-3} and its thickness varied between 0.05 and 0.5 µm.

The quantum efficiencies of the PD without the DBL and the PD with the DBL at 300 K and 200 K under zero bias are presented in Figure 6. For the typical $In_{0.83}Ga_{0.17}As$ PD without the DBL, the simulated peaks of the quantum efficiencies were found to be 69.6% at 2.5 µm at 300 K and 62.0% at 2.5 µm at 200 K. In Ref. [32], 1280 × 1024 focal plane arrays for typical $In_{0.83}Ga_{0.17}As$ PDs were measured on a 40 × 40 backside-illuminated array by adopting a Fourier transform infrared method at 180 K, and the peak of the quantum efficiency was recorded as 69% at 2.2 µm [32]. The simulated results are slightly different from the experimental one, perhaps due to the different hole lifetimes and mobilities used in the simulation. However, the difference is within an acceptable range.

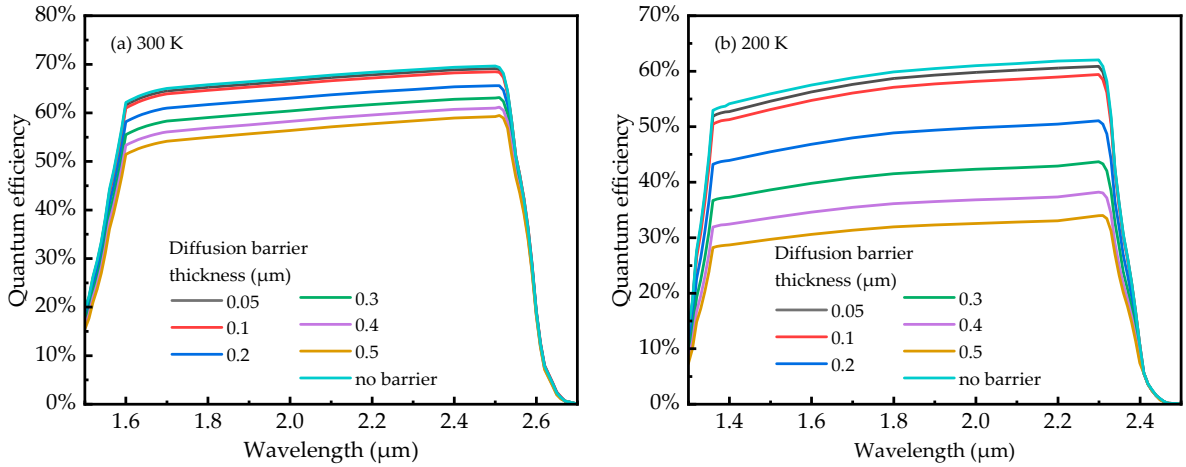

Figure 6. The simulated quantum efficiency of the $In_{0.83}Ga_{0.17}As/InP$ PD with the DBL doped at 5×10^{16} cm^{-3} at (**a**) 300 K and (**b**) 200 K.

As seen from Figure 6, the quantum efficiency is lower for the PD with the DBL than for the PD without the DBL at both temperatures. Quantum efficiency also decreases with increasing DBL thickness and doping concentration, as shown in Figure 7. The lowered quantum efficiency could be attributed to three reasons. Firstly, as illustrated in the band diagram of Figure 2, the DBL introduces an unfavorable impediment for hole collection, leading to a decrease in quantum efficiency. Secondly, the higher-doped DBL also results in a reduction in the width of the depletion region, consequently diminishing the capacity to collect photogenerated carriers. In Figure 8, the electron and doping concentrations at various diffusion barrier thicknesses under zero bias at 300 K are shown, which can be used to determine the width of the depletion region. In the depletion region, the impurities are ionized and become completely ionized when the electron concentration coincides with the doping concentration. The depletion regions in the $In_{0.83}Ga_{0.17}As$ layers are illustrated by the blue areas in the figure. It is shown in the figure that the width of the depletion region decreased from 0.5 to 0.18 μm when the DBL increased from 0.05 to 0.2 μm. When the DBL is further increased from 0.2 to 0.5 μm, the width of the depletion region remains unchanged at 0.18 μm.

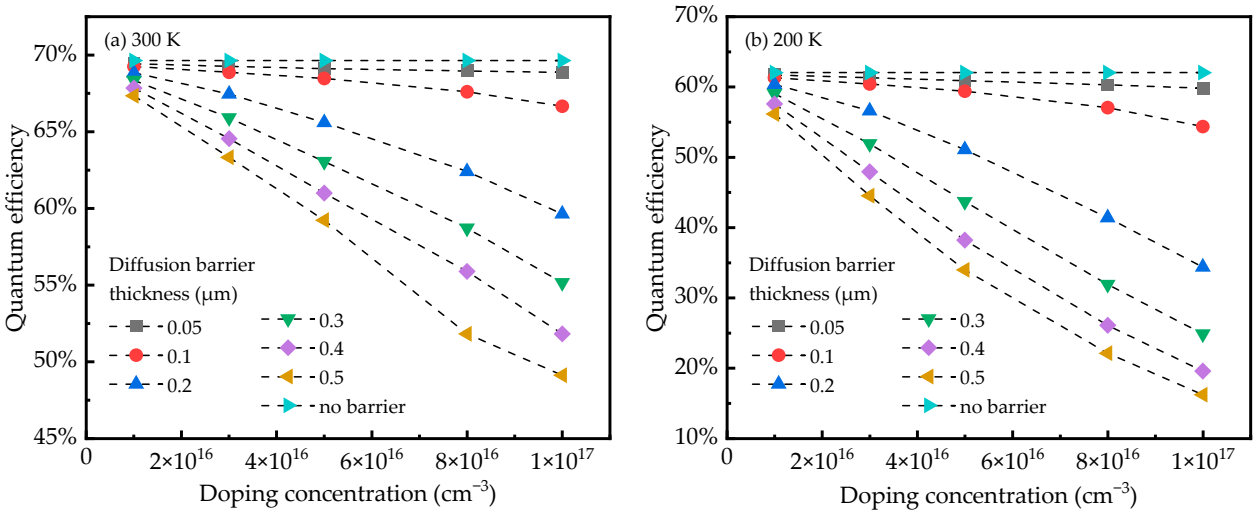

Figure 7. The influence of thickness and the doping concentration of the DBL on quantum efficiency at (**a**) 300 K and (**b**) 200 K.

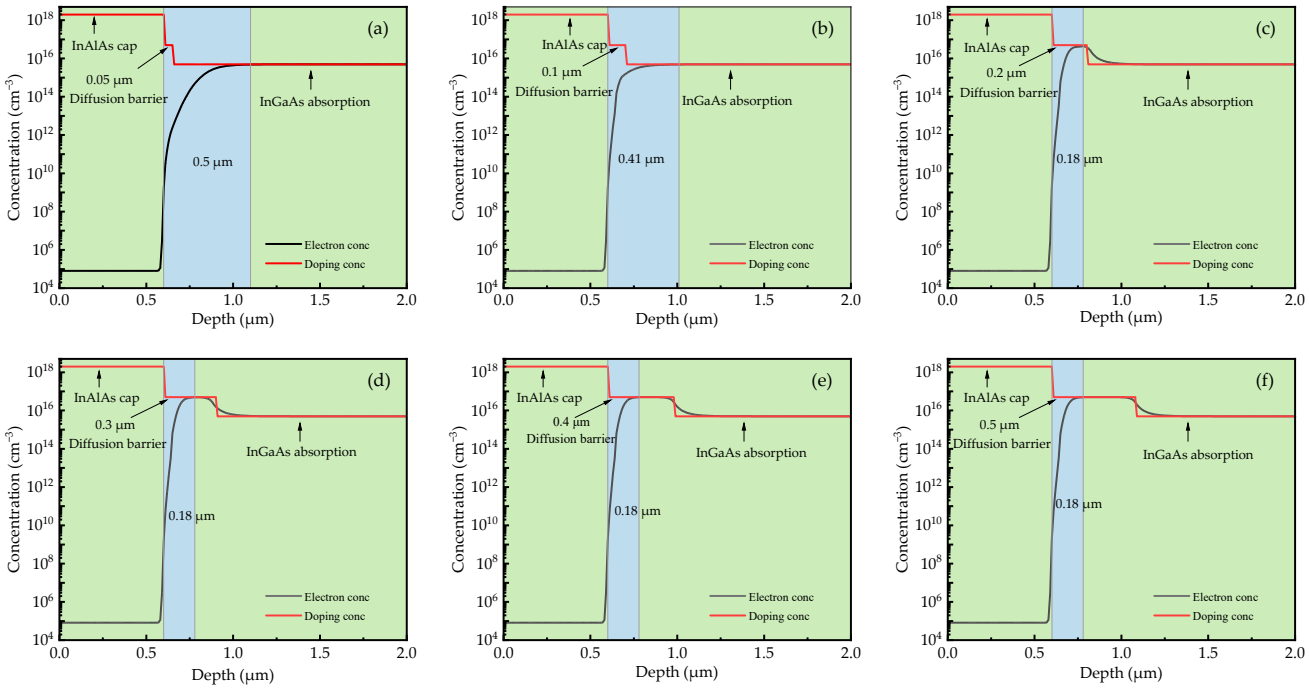

Figure 8. Electron and doping concentrations for the PD with different thicknesses of DBL at the doping concentration of 5×10^{16} cm^{-3} under zero bias at 300 K. The blue area represents the depletion region in the DBL and the $In_{0.83}Ga_{0.17}As$ absorption layer. The widths of the depletion region and the thicknesses of the DBL are marked on each of the figure (**a**–**f**).

Furthermore, as the doping concentration of the DBL increases, the minority carrier lifetime (τ_p) experiences a notable reduction [21]. The reduced τ_p value could result in diminished diffusion length according to the relationship of $L_P = \left(D_P \tau_p\right)^{1/2}$, where L_P is the diffusion length and D_P is the diffusion coefficient. The decrease in quantum efficiency as well as diffusion length is more noticeable at the lower temperature of 200 K [31].

Based on the above analysis, a thick and highly doped DBL could result in very low quantum efficiency. From the perspective of quantum efficiency, we suggest the doping concentrations of the DBL be between 1×10^{16} and 8×10^{16} cm^{-3} and that the thickness be between 0.05 and 0.1 μm.

3.4. Capacitance

An increase in capacitance can be a limiting factor for applications requiring rapid response and high bandwidth. As shown above, inclusion of the DBL alters the width of the depletion region, ultimately impacting the capacitance of the device [33]. Thus, it is necessary to investigate the effect of the DBL on the capacitance of the PD through simulation.

As illustrated in Figure 9, the reverse bias-dependent capacitances of the PD with the DBL at 300 K were simulated. The thickness of the DBL was changed while the concentration was fixed at 5×10^{16} cm^{-3}. The simulated capacitance of the PD without the DBL at 300 K is also shown in the figure, and its value is 42.3 nF/cm^2 at zero bias. In Ref. [34], the measured capacitance at 0 V bias in the experimental structure was 99.2 nF/cm^2 and 106.7 nF/cm^2 for $In_{0.8}Ga_{0.2}As$ absorption layers doped at 3×10^{16} cm^{-3} and 1×10^{17} cm^{-3}, respectively [34]. The simulated value is in the same order of magnitude as the measured ones.

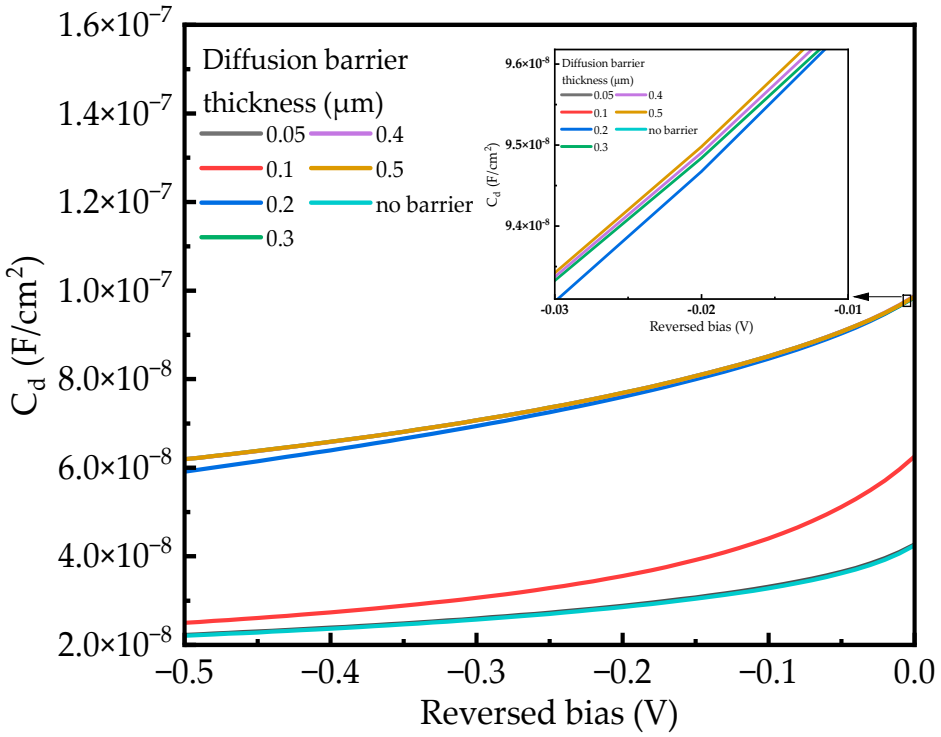

Figure 9. The capacitance C_d as a function of the reversed bias for different thicknesses of DBL at the doping concentration of 5×10^{16} cm^{-3} at 300 K. The inset shows an enlarged view of the overlapped curves.

Additionally, all the curves in Figure 9 show a decreasing trend with increased reversed bias, though at a slower rate when reversed bias is further increased, likely related to the change in depletion width. The capacitance also becomes bigger as the thickness of the DBL increases. The increase in capacitance is most significant when the thickness of the DBL changes from 0.1 to 0.2 μm, corresponding to the decrease in depletion width from 0.41 to 0.18 μm in the absorption layer, as shown in Figure 8. Beyond that, capacitance only exhibits a small increase because the depletion width is maintained at 0.18 μm, as shown in Figure 8.

Besides thickness, the doping concentration of the DBL also has an effect on capacitance. The capacitance C_d is described by the following equations:

$$C_d = \frac{\varepsilon A}{W}, \tag{1}$$

$$W = \left[\frac{2\varepsilon(V_b + V)}{qN_d}\right]^{\frac{1}{2}}, \tag{2}$$

In the equations, ε is the permittivity of InGaAs, W is the depletion width, A is the area of contact between the depletion region of the N- and P- zones, V is the bias voltage, V_b is built-in voltage, and N_d is the doping concentration of N- zones. Thus, increasing the doping concentration N_d in the N- zones will also shorten the depletion width and increase the capacitance. Figure 10 displays the capacitances at different doping concentrations with a 0.1 μm thick DBL in the PD at 300 K and 200 K. Notably, when the doping concentration exceeds 5×10^{16} cm^{-3}, there is a significant surge in capacitance at both temperatures. Given the behavior of the capacitance, we suggest that the DBL remains below 0.1 μm and that the doping concentrations be between 1×10^{16} and 5×10^{16} cm^{-3}.

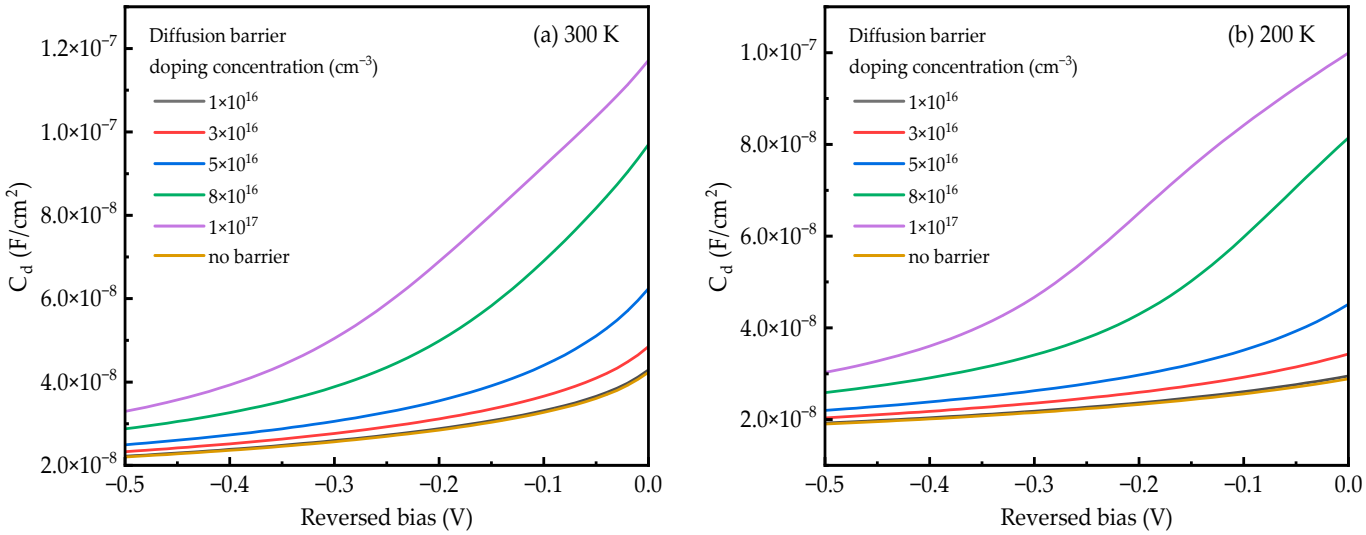

Figure 10. The capacitance C_d as a function of the reversed bias at different doping concentrations for the 0.1 μm thick DBL at (**a**) 300 K and (**b**) 200 K.

Considering dark current, quantum efficiency, and capacitance, the concentration of the DBL is best between 3×10^{16} and 5×10^{16} cm^{-3} at a thickness of 0.1 μm. With the DBL, the dark current is slightly reduced and the capacitance increased a little bit, the same tendency as observed in lattice-matched InGaAs/InP PDs with DBLs [19,35], indicating the validity of our simulation. Experiments will be further conducted with the optimized DBL thickness and doping concentration.

4. Conclusions

In this paper, a low-doped lattice-mismatched metamorphic $In_{0.83}Ga_{0.17}As$/InP PD with an n-type $In_{0.83}Ga_{0.17}As$ DBL was simulated using Silvaco TCAD. The simulated results of the PD without the DBL were compared to experimental measurements to confirm the validity of the simulation process. The I-V, quantum efficiency, and C-V characteristics of the PDs with various thicknesses and doping concentrations of DBL were investigated at the temperatures of 300 K and 200 K. Our analysis reveals that the introduction of the DBL modifies the energy band diagram, reduces the depletion width, and thus impacts PD performance. The dark current generally becomes smaller with thicker DBLs, though at a rate that decrease more slowly for high doping concentrations. Quantum efficiency decreased significantly when the thickness of the DBL exceeded 0.1 μm and when doping concentration was higher than 8×10^{16} cm^{-3}. Regarding capacitance, a minimal increase was observed when the thickness of the DBL was less than 0.1 μm and when doping was below 5×10^{16} cm^{-3}. Therefore, considering all these factors, for better PD performance, it is preferred that the concentration of the DBL be between 3×10^{16} and 5×10^{16} cm^{-3} and that the thickness be 0.1 μm. The optimal thickness and doping concentration as indicated by the simulation results could help towards improvements in lattice-mismatched metamorphic $In_{0.83}Ga_{0.17}As$ PDs with a planar configuration.

Author Contributions: Conceptualization, Z.J. and Y.G.; methodology, Z.J. and T.G.; software, Z.J. and T.G.; formal analysis, Z.J., T.G. and G.Z.; validation, Y.M. and Y.Y.; investigation, B.L., Y.Y. and C.Y.; resources, Y.G., B.L. and Y.M.; writing—original draft preparation, Z.J. and T.G.; writing—review and editing, Z.J., T.G. and Y.G.; supervision, Y.G.; funding acquisition, Z.J., Y.G., T.L. and X.L. All authors have read and agreed to the published version of the manuscript.

Funding: This research was funded by the National Natural Science Foundation of China (grant numbers 61704103, 62274169, and 62075229), the National Key R&D Program (grant numbers 2023YFF0713602 and 2022YFB3904803), the Program of Shanghai Academic/Technology Research Leader (grant number 21XD1404200), the Shanghai Rising Star Program (grant number 21QA1410600),

and the International Science and Technology Cooperation Program of Shanghai (grant number 20520711200).

Data Availability Statement: The data presented in this study are available on request from the corresponding author.

Conflicts of Interest: The authors declare no conflicts of interest.

References

1. Malchow, D.; Battaglia, J.; Brubaker, R.; Ettenberg, M. High speed short wave infrared (SWIR) imaging and range gating cameras. In Proceedings of the Thermosense XXIX, Orlando, FL, USA, 9–12 April 2007; SPIE: Bellingham, WA, USA, 2007; Volume 6541, p. 654106.
2. Zha, J.; Luo, M.; Ye, M.; Ahmed, T.; Yu, X.; Lien, D.H.; He, Q.; Lei, D.; Ho, J.C.; Bullock, J.; et al. Infrared Photodetectors Based on 2D Materials and Nanophotonics. *Adv. Funct. Mater.* **2021**, *32*, 2111970. [CrossRef]
3. Thimsen, E.; Sadtler, B.; Berazin, M.Y. Shortwave-infrared (SWIR) emitters for biological imaging: A review of challenges and opportunities. *Nanophotonics* **2017**, *6*, 1043–1054. [CrossRef]
4. Liu, H.Z.; Wang, J.Y.; Guo, D.Q.; Shen, K.; Chen, B.L.; Wu, J. Design and Fabrication of High Performance InGaAs near Infrared Photodetector. *Nanomaterials* **2023**, *13*, 2895. [CrossRef]
5. Hoogeveen, R.W.M.; Van der A, R.J.; Goede, A.P.H. Extend wavelength InGaAs infrared (1.0–2.4 μm) detector arrays on SCIAMACHY for space-based spectrometry of the Earth atmosphere. *Infrared Phys. Technol.* **2001**, *42*, 1–16. [CrossRef]
6. Smiri, B.; Arbia, M.B.; Ilkay, D.; Saidi, F.; Othmen, Z.; Dkhil, B.; Ismail, A.; Sezai, E.; Hassen, M. Optical and structural properties of In-rich $In_xGa_{1-x}As$ epitaxial layers on (100) InP for SWIR detectors. *Mater. Sci. Eng. B* **2020**, *262*, 114769. [CrossRef]
7. Kwan, C.; Chou, B.; Yang, J.; Rangamani, A.; Tran, T.; Zhang, J.; Etienne-Cummings, R. Target tracking and classification using compressive sensing camera for SWIR videos. *Signal Image Video Process.* **2019**, *13*, 1629–1637. [CrossRef]
8. Adomeit, U.; Krieg, J. Shortwave infrared for night vision applications: Illumination levels and sensor performance. In Proceedings of the Optics in Atmospheric Propagation and Adaptive Systems XVIII, Toulouse, France, 22 September 2015; SPIE: Bellingham, WA, USA, 2015; Volume 9641, pp. 16–27.
9. Hoffman, A.; Sessler, T.; Rosbeck, J.; Acton, D.; Ettenberg, M. Megapixel InGaAs arrays for low background applications. In Proceedings of the Infrared Technology and Applications XXXI, Orlando, FL, USA, 28 March–1 April 2005; SPIE: Bellingham, WA, USA, 2005; Volume 5783, pp. 32–38.
10. Jurczak, P.; Sablon, K.A.; Gutierrez, M.; Liu, H.Y.; Wu, J. 2.5-μm InGaAs photodiodes grown on GaAs substrates by interfacial misfit array technique. *Infrared Phys. Technol.* **2017**, *81*, 320–324. [CrossRef]
11. D'Hondt, M.; Moerman, I.; Demeester, P. Dark current optimization for MOVPE grown 2.5 μm wavelength InGaAs photodetectors. *Electron. Lett.* **1998**, *34*, 910–912. [CrossRef]
12. Qu, X.; Bao, H.; Hanieh, S.; Xiong, L.; Zhen, H. An InGaAs graded buffer layer in solar cells. *J. Semicond.* **2014**, *35*, 014011. [CrossRef]
13. Park, S.; Kim, Y.; Nguyen, P.D.; Jeon, J.; Chun, B.S.; Lee, S.J. Toward Ga-free wavelength extended 2.6 μm InAsP photodetectors with high performance. *Adv. Funct. Mater.* **2023**, *34*, 2309897. [CrossRef]
14. Cao, P.; Wang, T.C.; Peng, H.L.; Zhuang, Q.D.; Zheng, W.H. Growth and dark current analysis of GaSb- and InP-Based metamorphic $In_{0.8}Ga_{0.2}As$ photodetectors. *Materials* **2023**, *16*, 4538. [CrossRef] [PubMed]
15. Lv, J.B.; Chen, J. Simulation of dark current suppression in p-i-n InGaAs photodetector with $In_{0.66}Ga_{0.34}As$/InAs superlattice electron barrier. *Infrared Phys. Technol.* **2016**, *77*, 335–338. [CrossRef]
16. Zhong, H.; Li, C.; Guo, D.Q.; Cheng, K.M.; Tang, X.Y.; Shen, K.; Wu, J. High performance $InAs_{0.91}Sb_{0.09}$ MWIR detectors with an AlAs1-ySby graded barrier. *Infrared Phys. Technol.* **2023**, *130*, 104584. [CrossRef]
17. Yuan, Q.; Guo, D.Q.; Cui, X.Y.; Tang, X.Y.; Shen, K.; Wu, J.; Wang, Z.M. High-performance midwave type-II superlattice infrared photodetectors with a stepped InAs/GaSb absorber. *IEEE Trans. Electron Devices* **2023**, *70*, 2347–2351. [CrossRef]
18. Cao, J.S.; Li, T.; Wang, H.Z.; Yu, C.L.; Yang, B.; Ma, Y.J.; Shao, X.M.; Li, X.; Gong, H.M. Study on InP/InGaAs hetero-structure detector with unintentionally doping absorption layer. *Infrared Laser Eng.* **2021**, *50*, 20210073.
19. Cao, J.S.; Yu, Y.Z.; Li, T.; Yu, C.L.; Gu, Y.; Yang, B.; Ma, Y.J.; Shao, X.M.; Li, X.; Gong, H.M. Lightly doped In0.53Ga0.47As/InP SWIR photodetectors with diffusion barrier structure. *Infrared Phys. Technol.* **2024**, *137*, 105112. [CrossRef]
20. Ettenberg, M.H.; Lange, M.J.; Sugg, A.R.; Cochen, M.J.; Olsen, G.H. Zinc diffusion in InAsP/InGaAs heterostructures. *J. Electron. Mater.* **1999**, *28*, 1433–1439. [CrossRef]
21. Zhou, L.; Zhang, Y.G.; Gu, Y.; Ma, Y.J.; Chen, X.Y.; Xi, S.P.; Li, H.S.B.Y. Effects of material parameters on the temperature dependent spectral response of $In_{0.83}Ga_{0.17}As$ photodetectors. *J. Alloys Comp.* **2015**, *619*, 52–57. [CrossRef]
22. Metzger, W.K.; Wanlass, M.W.; Ellingson, R.J.; Ahrenkiel, R.K.; Carapella, J.J. Auger recombination in low-band-gap n-type InGaAs. *Appl. Phys. Lett.* **2001**, *79*, 3272–3274. [CrossRef]
23. *Atlas User's Manual*; SILVACO International: Santa Clara, CA, USA, 2007.
24. Vurgaftman, I.; Meyer, J.R.; Ram-Mohan, L.R. Band parameters for III-V compound semiconductors and their alloys. *J. Appl. Phys.* **2001**, *89*, 5815–5875. [CrossRef]

25. Lee, H.J.; Gamel, M.M.A.; Ker, P.J.; Jamaludin, M.Z.; Wong, Y.H.; Yap, K.S.; Willmott, J.R.; Hobbs, M.J.; David, J.P.R.; Tan, C.H. Deriving the absorption coefficients of lattice mismatched InGaAs using genetic algorithm. *Mater. Sci. Semicond. Optoelectron.* **2008**, *153*, 107135. [CrossRef]
26. Kao, Y.C.; Chou, H.M.; Hsu, S.C.; Lin, A.; Lin, C.C.; Shih, Z.H.; Chang, C.L.; Hong, H.F.; Horng, R.H. Performance comparison of III-V//Si and III-V//InGaAs multi-junction solar cells fabricated by the combination of mechanical stacking and wire bonding. *Sci. Rep.* **2019**, *9*, 4308. [CrossRef] [PubMed]
27. Gamel, M.M.A.; Ker, P.J.; Rashid, W.E.S.W.A.; Lee, H.J.; Hannan, M.A.; Jamaludin, M.Z. Performance of Ge and $In_{0.53}Ga_{0.47}As$ thermophotovoltaic cells under different spectral irradiances. *IEEE Access* **2021**, *9*, 37091–37102. [CrossRef]
28. Roura, P.; Lopez-de Miguel, M.; Cornet, A.; Morante, J.R. Determination of the direct band-gap energy of InAlAs matched to InP by photoluminescence excitation spectroscopy. *J. Appl. Phys.* **1997**, *81*, 6916–6920. [CrossRef]
29. Chen, W.; Chen, B.; Yuan, J.; Holmes, A.; Fay, P. Bulk and interfacial deep levels observed in $In_{0.53}Ga_{0.47}As/GaAs_{0.5}Sb_{0.5}$ multiple quantum well photodiode. *Appl. Phys. Lett.* **2012**, *101*, 5.
30. Besikci, C. Extended short wavelength infrared FPA Technology: Status and trends. In Proceedings of the Quantum Sensing and Nano Electronics And Photonics XV, San Francisco, CA, USA, 28 January–2 February 2018; SPIE: Bellingham, WA, USA, 2018; Volume 10540, pp. 110–125.
31. Circir, K.; Dolas, M.H.; Kocaman, S. Optimization of in-device depleted passivation layer for InGaAs photodetectors. *Infrared Phys. Technol.* **2019**, *97*, 360–364. [CrossRef]
32. Cheng, J.F.; Li, X.; Shao, X.M.; Li, T.; Ma, Y.J.; Gu, Y.; Deng, S.Y.; Zhang, Y.G.; Gong, H.M. 2.45-μm 1280 × 1024 InGaAs focal plane array with 15-μm pitch for extend SWIR imaging. *IEEE Photon. Technol. Lett.* **2022**, *34*, 231–234. [CrossRef]
33. Geske, J.; Hood, A.; Thomas, J.; MacDougal, M. Low-capacitance InGaAs detectors for high-speed, wide field-of-view sensing applications. In Proceedings of the Infrared Technology and Applications XLV, Baltimore, MD, USA, 14–18 April 2019; SPIE: Bellingham, WA, USA, 2019; p. 11002.
34. Zhang, Y.G.; Gu, Y.; Tian, Z.B.; Li, A.Z.; Zhu, X.R.; Zhang, Y.L. Wavelength extended 2.4 μm heterojunction InGaAs photodiodes with InAlAs cap and linearly graded buffer layers suitable for both front and back illuminations. *Infrared Phys. Technol.* **2008**, *51*, 316–321. [CrossRef]
35. Djedidi, A.; Rouvie, A.; Reverchon, J.L.; Pires, M.; Chevalier, N.; Mariolle, D. Investigation of the influence of Zn-diffusion profile on the electrical properties of InGaAs/InP photodiodes. In Proceedings of the 2012 International Conference on Indium Phosphide and Related Materials, Santa Barbara, CA, USA, 27–30 August 2012; pp. 110–112.